Optimization with Partial Differential Equation Constraints for Bio-imaging Applications

Randolph E. Bank · **Yiqian Wu** · **Yiwen Shi** · **Philip E. Gill** · **Yingxiao Wang** · **Shaoying Lu**

Abstract Molecular transport and interaction are of fundamental importance in biology and medicine. The spatiotemporal diffusion map can reflect the regulation of molecular interactions and their intracellular functions. To construct subcellular diffusion maps based on bio-imaging data, we explore a general optimization framework with diffusion equation constraints (OPT-PDE). For the solution of the spatially piecewise constant and anisotropic diffusion tensors, we develop an efficient block solver based on applying Newton's method to the first-order necessary condition for optimality. We characterize the wellposedness of the OPT-PDE model problem and the convergence properties of the solver. We also demonstrate the general utility of the solver in recovering spatially heterogeneous and anisotropic diffusion maps with computer-simulated bio-images. The results indicate that the solver can accurately recover piecewise-constant isotropic and anisotropic diffusion coefficients, while exhibiting efficient convergence and robustness. This work highlights the power of the OPT-PDE model and the solver in recovering the diffusion map from imaging data, and demonstrates that it has significant implications in bio-imaging analysis.

Bank: Department of Mathematics, University of California, San Diego, La Jolla, California 92093-0112. Email:rbank@ucsd.edu
Wu: Department of Bioengineering, Department of Mathematics, University of California, San Diego, La Jolla, California 92093-0435. Email:y5wu@ucsd.edu
Shi: Department of Mathematics, University of California, San Diego, La Jolla, California 92093-0112. Email:yis018@ucsd.edu
Gill: Department of Mathematics, University of California, San Diego, La Jolla, California 92093-0112. Email:pgill@ucsd.edu
Wang: Department of Bioengineering, Department of Mathematics, University of California, San Diego, La Jolla, California 92093-0435. Email:yiw015@ucsd.edu
Lu: Department of Bioengineering, Department of Mathematics, University of California, San Diego, La Jolla, California 92093-0435. Email:kalu@ucsd.edu

1 Introduction

Molecular diffusion and transport is of fundamental importance in cell biology [9,20]. Diffusion and transport of a given molecule vary at different subcellular locations and can represent its local activity and function. Therefore, the spatiotemporal diffusion map can reflect the regulation of molecular interactions and their intracellular functions [35, 8,13]. However, the construction of subcellular diffusion maps based on image data remains a tremendous challenge [25,7].

Traditional diffusion analysis approaches by fluorescence recovery after photobleaching (FRAP) suffers from low spatiotemporal resolution, with significant limitations on the experimental photobleaching protocols [1,21,23]. To

overcome some of these limitations, fluorescence correlation spectroscopy (FCS) methods have been used to analyze the diffusion process in live cells [7,40]. Nevertheless, the spatial resolutions remain relatively low, and FCS methods can only handle images of low molecular density, and estimate the diffusion rate of a subpopulation of intracellular molecules. [7]. In contrast, model-based methods such as finite difference or finite element methods have the advantage of being theoretically well-defined, with high spatiotemporal resolution and less limitation on molecular density. These methods have been applied to study spatially homogeneous apparent molecular diffusion in live cells and tissues by the authors and others, respectively [25,36]. In this work, we develop a general optimization framework with diffusion equation constraints (OPT-PDE) and finite element discretization, with the goal of solving spatiotemporal heterogeneous and anisotropic diffusion maps based on live-cell FRAP images.

OPT-PDE models are extremely versatile, with applications ranging from biology, geophysics, aerodynamics, and finance [15,14,38]. However, the formulation and solution of OPT-PDE model problems are usually individualized and dependent on the specific applications involved. Therefore, it is important to develop the well-posedness theoretical framework for each application. The analytic optimality theory for OPT-PDE problems is usually posed in terms of operators defined on reflective Banach spaces with $\mathcal{L}^p$ norms and inner products [16,12]. Thus, functional analysis theory on Banach spaces, the existence and stability results of the PDE constraints, the weak smoothness of the objective functional, and the weak compactness of the Banach space of the state and control functions, are essential to guarantee the existence of optimal solutions and the optimality conditions [16,12,6].

The optimization problem in our application is to minimize a quadratic objective functional subject to a PDE with an unknown piecewise constant diffusion map. With time-space discretization of the PDE, good estimates of the first and second derivatives of the discretized problem can be computed with ease. Therefore, we utilize the modern *discretize-then-optimize* approach to solve the optimization model, with all the finite element unknowns of the PDE as variables [17,3]. As a result, the discrete optimization problem has a large number of variables and constraints that cannot be handled efficiently by conventional general-purpose optimization algorithms and software [26,11]. In order to deal with this difficulty, the proposed optimization algorithm is specifically designed to exploit the special structure in the derivatives of the differential-equation constraints. The OPT-PDE model was solved at the outer layer by Newton's method applied to the first-order necessary condition for optimality. At the inner layer, the large-scale linear system was solved by block elimination, while the sub-block linear system derived from the PDE was iteratively solved by an efficient preconditioner [16,2].

In this work, we formulate a general OPT-PDE model problem for our applications and examine the theoretical foundation of the well-posedness of the model problem. We develop a new OPT-PDE solver algorithm for inversely recovering spatially heterogeneous diffusion tensors from concentration maps, and implement different biologically motivated test problems generated by simulation. With the numerical solution of these test problems, we demonstrate that the proposed algorithm converges efficiently and recovers the underlying diffusion tensors with high accuracy. Thus, this general OPT-PDE model and solution framework can provide a new and important approach to recover spatially different diffusion coefficients and diffusion tensors from bio-images.

2 Optimization model with partial differential equation constraints

2.1 The Model Problem

An OPT-PDE model was formulated to estimate diffusion maps based on fluorescence images. The time-evolution of fluorescence images of live cells are usually recorded by microscope to represent the spatiotemporal distribution of molecular concentration $u(x,t)$. The concentration maps at given time points t_1 and t_2 are known functions $u_1(x)$ and $u_2(x)$ of space. It is assumed that the time-evolution of sequential fluorescence images is caused by the diffusion of fluorescent molecules with an unknown diffusion coefficient map $d(x)$, which is a piecewise constant tensor function of space. The system of differential equations is given by

$$\begin{cases} \dfrac{\partial u(x,t)}{\partial t} = \nabla \cdot (d(x)\nabla u(x,t)) \\ u(x,t_1) = u_1(x) \\ u(x,t_2) = u_2(x), \end{cases}$$

for all $x \in \Omega \subset \mathbb{R}^2$ or $\mathbb{R}^3$, and $t \in [t_1,t_2]$.

The inverse problem for the diffusion map $d(x)$ is formulated as a PDE-constrained optimization problem, where the objective function includes the $\mathcal{L}^2$ norms of $u - u_2$ and $d - d_0$. The initial value problem is imposed as an equality constraint. This gives a problem in which the objective function

$$\Phi(u(\cdot,t_2),d) = \int_\Omega (u - u_2)^2 + \gamma(d - d_0)^2 dx \qquad \text{(Eq 2.1)}$$

is minimized subject to the constraints $u(x,t_1) = u_1$, and

$$\nabla \cdot (d(x)\nabla u) = \frac{\partial u}{\partial t}, \text{ for } x \in \Omega \text{ and } t_1 < t \le t_2, \qquad \text{(Eq 2.2)}$$

with the homogeneous Neumann boundary conditions

$$d(x)\nabla u \cdot \mathbf{n} = 0, \text{ for } x \in \partial \Omega, \text{ and } t_1 < t \le t_2.$$

Here the unit vector $\mathbf{n}$ is the outward normal on the boundary $\partial \Omega$. The diffusion coefficient map function is piecewise constant and bounded above and below by the box constraint,

$$0 < d_{\min} \le d(x) \le d_{\max}. \tag{Eq 2.3}$$

In the objective function (Eq 2.1), the Tikhonov regularization term $\gamma(d - d_0)^2$ is needed to ensure the well-posedness of the optimization problem, and to allow the efficient solution of the linear system defined by the numerical discretization [37,33]. The scalar γ is chosen as a small constant of order 10^{-5} to provide the needed regularization while not forcing the diffusion coefficient to the initial guess d_0. A disadvantage of the regularization term is that it can limit the accuracy of the solution by forcing the diffusion coefficients to converge to a point near d_0. However, a more accurate solution is possible if a sequence of problems are solved in which the solution of one problem is used for the regularization term d_0 of the next. This method with modified Tikhonov regularization terms is similar to the proximal-point method for nonlinear optimization (see, e.g., [29,34]). The benefits of this approach are illustrated in Section 4.

The PDE constraint (Eq 2.2) is approximated in time using the backward difference

$$\nabla \cdot (d\nabla u) = \frac{u - u_1}{\Delta t},$$

or, equivalently,

$$-\nabla \cdot (d\nabla u) + (\Delta t)^{-1} u = (\Delta t)^{-1} u_1.$$

This gives the weak form of the PDE constraint as: find $u \in \mathcal{H}^1(\Omega)$ such that

$$\begin{aligned} a(u,v) &\equiv \int_\Omega d\nabla u \cdot \nabla v + (\Delta t)^{-1} uv \, dx \\ &= \int_\Omega (\Delta t)^{-1} u_1 v \, dx \equiv \left((\Delta t)^{-1} u_1, v\right) \end{aligned}$$

for all $v \in \mathcal{H}^1(\Omega)$. Let $\mathcal{S}_h \subset \mathcal{H}^1(\Omega)$ denote the finite element space consisting of continuous piecewise linear polynomials associated with a shape regular triangulation $\mathcal{T}_h$ of Ω. The discrete bilinear form can be written as: find $u^h \in \mathcal{S}_h$ such that

$$a(u^h, v^h) = \left((\Delta t)^{-1} u_1, v^h\right) \text{ for all } v^h \in \mathcal{S}_h. \tag{Eq 2.4}$$

Several observations may be made regarding the discretization process. Although the test examples are generated through simulation, in practice the data comes from live cell images, in which case the solutions u_1, u_2, the shape of the domain Ω as well as its internal geometric details

will be limited by the image resolution. As these data are derived from point (pixel) values of the images, the use of low-order finite elements is natural and appropriate in this setting. The use of simple backward difference for the time discretization is also appropriate for the same reason. Here Δt is a constant bounded below and away from zero such that $(\Delta t)^{-1}$ remains bounded above. Practical problems will likely have more than two data points in time; in anticipation of this, we note that the objective function can be generalized by summing over multiple time steps. The time discretization can also be extended to cover the case of multiple time steps. However, in this study, our main goal is to validate the convergence and efficiency of the overall optimization approach, and thus we present a simplified version of the time evolution problem.

2.2 The well-posedness of the PDE

As the bilinear form $a(\cdot, \cdot)$ is symmetric, uniformly bounded above and below (i.e., uniformly elliptic, see (Eq 2.3)), the Riesz representation theorem gives the existence and uniqueness of the solution [16,6]. In this case, the right-hand side function $f(x) = (\Delta t)^{-1} u_1(x)$ is in $\mathcal{L}^2(\Omega)$. The theory allows that the function $f(x)$ be discontinuous at an internal interface between subdomains within Ω [16,6].

Elliptic problems with discontinuous piecewise constant diffusion coefficients are also called Laplace-interface problems or transmission problems. The solutions of these problems possess characteristic singularities, with decreased regularity and low-order approximation errors in finite element applications [31]. The discontinuity of the diffusion coefficients implies that the solution u will not have the piecewise regularity $\mathcal{H}^2(\Omega_i)$ implied by the piecewise $\mathcal{L}^2$ property of the right-hand side.

In the numerical examples of Section 4, the domain Ω contains several subdomains, with discontinuous piecewise constant diffusion coefficients. Therefore, $\Omega = \cup_{k=1}^K \Omega_k$, and the diffusion map function $d(x) = d_k$ for $x \in \Omega_k$, and $k = 1, 2, \ldots, K$. The d_k's are either positive constants in $\mathbb{R}$, or symmetric positive-definite diffusion tensor matrices in $\mathbb{R}^{2\times 2}$. The weak form of the elliptic problem is to find u, such that for every test function v, the trilinear form satisfies $T(d,u,v) = 0$ [12], where

$$\begin{aligned} T(d,u,v) &\equiv \sum_{k=1}^K \int_{\Omega_k} \nabla u \cdot (d_k \nabla v) dx + \int_\Omega \frac{1}{\Delta t} uv \, dx \\ &- \int_\Omega \frac{1}{\Delta t} u_1 v \, dx = 0. \end{aligned} \tag{Eq 2.5}$$

Similar to the case of continuous constant diffusion coefficients, if d_k is uniformly bounded above and below (see (Eq 2.3)), or if d_k is a symmetric tensor matrix with eigenvalues that are uniformly bounded above and below, the weak

forms of elliptic problems with discontinuous diffusion coefficients have a unique solution [12,6].

The regularity properties for elliptic problems with discontinuous coefficients have been studied by Petzoldt in his thesis and two related papers [31,30,32]. The majority of regularity results depend on the so-called "quasi-monotonicity condition" [31,10], which requires that the diffusion coefficients around each singular point be traced in a monotonic order. In particular, the solution u is in $\mathcal{H}^{1+1/4}(\Omega_i)$ if and only if quasi-monotonicity is satisfied, with the bound shown to be optimal [31,30,19]. All the piecewise constant diffusion coefficients in our numerical examples are quasi-monotone.

The ratio between the upper and lower bounds of the diffusion coefficients may be regarded as a measure of problem "stiffness". If this ratio is bounded above and below by the uniform elliptic condition on the PDE operator, an iterative multigrid solver can achieve a convergence rate independent of the jumps in the diffusion coefficients [39,28,42], which is the case for the PDE solver used here.

2.3 The PDE-constrained optimization problem

Based on (Eq 2.1), the optimization problem is formulated with a PDE equality constraint, i.e.,

$$\min_{(u,d)\in U_{ccs}\times D_{ccs}} \Phi(u,d) = \int_{\Omega}(u-u_2)^2 + \gamma(d-d_0)^2 dxdy,$$

$$\text{subject to } e(u,d) \equiv \nabla\cdot(d\nabla u) - \frac{u-u_1}{\Delta t} = 0, \qquad \text{(Eq 2.6)}$$

where $U_{ccs} = \mathcal{H}^1(\Omega)$, and $D_{ccs} = \{d \in \mathcal{L}^\infty(\Omega), \text{ and } 0 < d_{\min} \le d \le d_{\max}\}$.

In weak form, the PDE constraint is the trilinear functional given by (Eq 2.5). The discrete OPT-PDE problem is then

$$\min_{(u^h,d^h)\in\mathbb{R}^N\times\mathbb{R}^N} \Phi(u^h,d^h) = (u^h-u_2^h)^T M(u^h-u_2^h)$$

$$+ \gamma(d^h-d_0^h)^T M(d^h-d_0^h)$$

$$\text{subject to } T(d,u^h,v^h) \equiv \left(\sum_{k=1}^{K} d_k A_k\right)u^h + \frac{M(u^h-u_1^h)}{\Delta t} = 0.$$

$$\text{(Eq 2.7)}$$

Here N is the number of nodes in the triangulation, which represents the degrees of freedom in the discrete linear system, and K is the number of non-overlapping subdomains $\Omega_k \subset \Omega$ with distinct diffusion coefficients. M is the finite element mass matrix, and A_k is the stiffness matrix corresponding to the subdomain Ω_k.

Based on the theory of invertible functions in Banach spaces [16,18,41], this optimization problem has a unique solution. In particular, it has been shown that the solution

of an elliptic boundary-value problem is an infinitely differentiable functional of the diffusion coefficients d, with a bounded d-derivative, and subsequently a bounded d-inverse [12]. When the objective function for the optimization is chosen as an energy norm that is dependent on the diffusion coefficients, it is a smooth and convex functional of the coefficients [12,43,22]. With this objective function the discontinuous coefficients are estimated from measured interior fluorescent intensity or molecular concentrations, by approximating the optimal solution in both continuous and discrete settings [12].

For the optimization of an objective function with PDE constraints in the setting of our bioimaging applications, the minimization problem

$$\min_{(u,d)\in U_{ccs}\times D_{ccs}} \Phi(u,d), \text{ such that } e(u,d) = 0,$$

has an optimal solution if three conditions are satisfied [16].

1. D_{ccs} is bounded, convex, and closed. U_{ccs} is convex and closed.
2. $\Phi(u,d)$ is sequentially weakly lower semi-continuous.
3. The PDE constraint $e(u,d) = 0$ is continuous under weak convergence and has a bounded d-inverse operator $e_d^{-1} : d \in D_{ccs} \mapsto u(d) \in U_{ccs}$.

For the continuous problem, U_{ccs} is the set of concentration functions, which is a closed subset of the Hilbert space $\mathcal{H}^1$ with norm and inner product. D_{ccs} is the set of diffusion coefficients, which is a bounded, convex, and closed subset of $\mathcal{L}^2$. Both U_{ccs} and D_{ccs} are Hilbert spaces and thus reflexive Banach spaces. It follows that condition (1) holds. In addition, Φ is quadratic in both u and d, so it is obviously continuous, and hence condition (2) is satisfied. Conditions (1) and (2) guarantee that Φ has an achievable infimum Φ^*, i.e., there is a minimizing sequence $\{(u_k,d_k)\} \subset U_{ccs}\times D_{ccs}$, such that $\Phi(u_k,d_k) \rightharpoonup \Phi^*$. As the convex and closed set D_{ccs} is bounded, the sequence $\{d_k\}$ has a weakly convergent subsequence $\{d_{k_i}\}$, such that $d_{k_i} \rightharpoonup d^*$. The equality constraint, $e(u,d)$ has a bounded d-inverse, which implies that condition (3) holds. It follows that if $u_{k_i} = e_u^{-1}(\cdot,d_{k_i})$ and $u^* = e_u^{-1}(\cdot,d^*)$ then it can be shown that $u_{k_i} \rightharpoonup u^*$. In addition, the objective function is quadratic, i.e., $\Phi(u_{k_i},d_{k_i}) \rightharpoonup \Phi^*$. Therefore, our continuous OPT-PDE problem has an optimal solution (u^*,d^*).

Similarly, for the discrete problem, U_{ccs} is the set of discrete concentration, which is the finite element discretization of a bounded, convex, and closed subset of the Hilbert space $\mathcal{H}^1$, or $\mathbb{R}^N$. D_{ccs} is the set of discrete diffusion coefficients, which is a convex, and closed subset of $\mathbb{R}^N$. This implies that both U_{ccs} and D_{ccs} are reflexive. In addition, $Z = \mathbb{R}^N$. Φ is quadratic in both u^h and d^h, so it is obviously weakly continuous. Because of the well-posedness and the

stability of the discrete PDE, the condition (3) is also satisfied. Therefore, the discrete OPT-PDE model problem has an optimal solution $(u^{h,*}, d^{h,*})$.

In summary, these results for the continuous and discrete problems imply that the solution of an optimization problem with a PDE constraint exists when the objective function Φ is weakly continuous, the domain of the constraint operator is a compact subset of Banach space, and the equality constraint contains a well-posed PDE with bounded d-inverse.

An alternative implementation of the objective function in the discrete OPT-PDE model is to normalize the diffusion coefficients by their magnitude in such a way that the convergence of the optimization problem and the error of solutions are independent of the values of diffusion coefficients. In this case, the discrete objective function becomes

$$\Phi_h(u^h, d^h) = \frac{1}{2}(u^h - u_2^h)^T M (u^h - u_2^h)$$
$$+ \frac{\gamma}{2} \sum_{k=1}^{K} \left(\frac{d_k - d_{0,k}}{d_{0,k}} \right)^2 \text{Area}(\Omega_k), \quad \text{(Eq 2.8)}$$

and the corresponding discrete OPT-PDE problem remains well-posed.

3 Description of the algorithm

The discrete OPT-PDE problem given by (Eq 2.7) can be solved by minimizing the Lagrangian function [26,2,5].

$$L(u, d, v) = \frac{1}{2}(u^h - u_2^h)^T M (u^h - u_2^h)$$
$$+ \frac{1}{2}\gamma (d^h - d_0^h)^T M (d^h - d_0^h)$$
$$+ u^{h,T}\left(\sum_{k=1}^{K} d_k A_k \right) v^h + \Delta t^{-1}(u^h - u_1^h)^T M v^h,$$

where A_k is the subdomain stiffness matrix. First, we consider the simple case where d_k is a scalar in each subdomain Ω_k, $k = 1, 2, \ldots, K$.

The Lagrangian function is minimized numerically by applying Newton's method to the first-order conditions [26, 2]. As the PDEs are solved to an accuracy that is finer than the convergence tolerance of the Newton iterations, we expect the usual theoretical rate of convergence of Newton's method for a system of nonlinear equations [27]. The gradient of the Lagrangian is $J = [\frac{\partial L}{\partial u}, \frac{\partial L}{\partial v}, \frac{\partial L}{\partial d}]^T$. The quadratic functional of the control variable d^h,

$$q(d^h - d_0^h) \equiv \frac{1}{2}\gamma (d^h - d_0^h)^T M (d^h - d_0^h),$$

can be simplified when $d^h = [d_1, d_2, \ldots, d_K]^T$ is a discrete piecewise constant function in space. In particular,

$$q(d^h - d_0^h) = \sum_{k=1}^{K} \frac{1}{2}\gamma S(M_k)(d_k - d_0)^2,$$

where $S(M_k)$ is the sum of all entries in the subdomain mass matrix M_k, for $k = 1, 2, \ldots, K$.

It follows that the gradient of the Lagrangian is

$$\frac{\partial L}{\partial d} = \begin{bmatrix} \gamma S(M_1)(d_1 - d_0) + u^{h,T} A_1 v^h \\ \vdots \\ \gamma S(M_K)(d_K - d_0) + u^{h,T} A_K v^h \end{bmatrix}.$$

The first-order necessary condition implies that the gradient of the Lagrangian functional is zero, i.e.,

$$\begin{cases} M(u^h - u_2^h) + A v^h = 0 \\ A u^h - M u_1^h / \Delta t = 0 \\ \partial L / \partial d = 0 \end{cases}$$

where $A = \sum_{k=1}^{K} d_k A_k + M/\Delta t$. The KKT matrix H (see, e.g., [26]) is given by

$$H = \begin{bmatrix} M & A & C_u \\ A & 0 & C_v \\ C_u^T & C_v^T & G \end{bmatrix},$$

where the submatrices $C_u = [A_1 v^h \cdots A_K v^h]$, $C_v = [A_1 u^h \cdots A_K u^h]$, and the diagonal matrix $G = \gamma \text{diag}[S(M_1), \ldots, S(M_K)]$. Observe that C_u and C_v may be rank deficient if the discrete Laplacian of u^h and v^h are both zero in a certain subregion. In this case, a nonzero γ is needed to guarantee the non-singularity of the KKT matrix and the well-posedness of the optimization problem. This notion will be further illustrated in the numerical results section.

In the general case, each d_k is a symmetric tensor matrix $d_k = \begin{bmatrix} d_{11,k} & d_{12,k} \\ d_{12,k} & d_{22,k} \end{bmatrix}$ in the subdomain Ω_k. In this case, the Lagrangian function is

$$L(u, d, v) = \frac{1}{2}(u^h - u_2^h) M (u^h - u_2^h) + q(d^h - d_0^h)$$
$$+ u^{h,T}\left(\sum_{k=1}^{K} A(d_k) \right) v^h + \Delta t^{-1}(u - u_1^h)^T M v^h.$$

The quadratic function $q(d^h - d_0^h)$ is

$$q(d^h - d_0^h) = \frac{1}{4}\gamma (d_{11}^h - d_{11,0}^h)^T M (d_{11}^h - d_{11,0}^h)$$
$$+ \frac{1}{2}\gamma (d_{12}^h - d_{12,0}^h)^T M (d_{12}^h - d_{12,0}^h)$$
$$+ \frac{1}{4}\gamma (d_{22}^h - d_{22,0}^h)^T M (d_{22}^h - d_{22,0}^h).$$

This definition of $q(d^h - d_0^h)$ is consistent with the scalar case where $d_k = \begin{bmatrix} d_{11,k} & 0 \\ 0 & d_{11,k} \end{bmatrix}$.

The subregion stiffness matrix $A_k(d_k)$ can be written as a linear combination of three terms corresponding to the 2nd-order derivatives of u in the Laplace operator, i.e.,

$$A_k(d_k) = d_{11,k}A_{11,k} + d_{12,k}A_{12,k} + d_{22,k}A_{22,k},$$

where $A_{11,k}$, $A_{12,k}$, and $A_{22,k}$ are stiffness matrices corresponding to the respective diffusion tensors

$$\begin{bmatrix} 1 & 0 \\ 0 & 0 \end{bmatrix}, \begin{bmatrix} 0 & 1 \\ 1 & 0 \end{bmatrix}, \text{ and } \begin{bmatrix} 0 & 0 \\ 0 & 1 \end{bmatrix}.$$

It follows that, the partial derivatives of q and A_k are

$$\frac{\partial q}{\partial d_{ij,k}} = \begin{cases} \frac{1}{2}\gamma M(d_{ij,k}^h - d_{ij,k,0}^h), & \text{when } i = j; \\ \gamma M(d_{ij,k}^h - d_{ij,k,0}^h), & \text{when } i \neq j, \end{cases}$$

and

$$\frac{\partial A_k(d_k)}{\partial d_{ij,k}} = A_{ij,k}.$$

This gives the first-order derivatives of the Lagrangian as

$$\frac{\partial L}{\partial d} = \begin{bmatrix} \vdots \\ \frac{1}{2}\gamma S(M_k)(d_{11,k} - d_{11,k,0}) + u^{h,T}A_{11,k}v^h \\ \gamma S(M_k)(d_{12,k} - d_{12,k,0}) + u^{h,T}A_{12,k}v^h \\ \frac{1}{2}\gamma S(M_k)(d_{22,k} - d_{22,k,0}) + u^{h,T}A_{22,k}v^h \\ \vdots \end{bmatrix}.$$

The block sub-matrices in the KKT matrix H have 3K columns, with

$$C_u = \begin{bmatrix} \cdots & A_{11,k}v^h, & A_{12,k}v^h, & A_{22,k}v^h & \cdots \end{bmatrix},$$

$$C_v = \begin{bmatrix} \cdots & A_{11,k}u^h, & A_{12,k}u^h, & A_{22,k}u^h & \cdots \end{bmatrix},$$

and

$$G = \text{diag} \begin{bmatrix} \cdots & \frac{1}{2}\gamma S(M_k), & \gamma S(M_k), & \frac{1}{2}\gamma S(M_k) & \cdots \end{bmatrix}.$$

In the numerical examples, the diffusion tensor is a 2×2 diagonal matrix with a known rotation matrix Q, i.e., $d_k = Q^T \begin{bmatrix} d_{11,k} & 0 \\ 0 & d_{22,k} \end{bmatrix} Q$. In this case, the matrices C_u and C_v have two columns corresponding to each such diffusion tensor in a subdomain, and the diagonal matrix G has two corresponding diagonal entries.

For both scalar and tensor diffusion, the Newton direction $p = [\delta u, \delta v, \delta d]^T$ at the jth step can be calculated using the linear system involving the KKT matrix and the negative gradient of the Lagrangian evaluated at the jth iterate [26].

$$Hp = -J(u^j, v^j, d^j) = - \begin{bmatrix} M(u^j - u^h{}_2) + Av^j \\ Au^j - Mu^h{}_1/\Delta t \\ (\partial L/\partial d)^j \end{bmatrix} \equiv - \begin{bmatrix} J_u \\ J_v \\ J_d \end{bmatrix}.$$

To simplify the notation, we drop the Newton iteration index j. At each Newton step, the Newton equations may be expressed in terms of the KKT equations [26], which are given by the block 3×3 linear system of the form

$$\begin{bmatrix} M & A & C_u \\ A & 0 & C_v \\ C_u^T & C_v^T & G \end{bmatrix} \begin{bmatrix} \delta u \\ \delta v \\ \delta d \end{bmatrix} = - \begin{bmatrix} J_u \\ J_v \\ J_d \end{bmatrix}. \qquad \text{(Eq 3.1)}$$

(Normally such KKT systems are expressed in block 2×2 form with the zero block as the lower-right diagonal.) In this case, we wish to exploit the special sparse structure of the mass matrix M and stiffness matrix A, with A being positive definite. The corresponding equation can be solved efficiently by many standard iterative methods. In addition, the block matrices C_u and C_v are rectangular sub-matrices consisting of column vectors, and G is a low-dimensional diagonal matrix. Each block system is solved using a variant of block Gaussian elimination that exploits existing efficient solvers for the linear systems with matrix A. Starting with block factorization, the matrix

$$\begin{bmatrix} M & A & C_u \\ A & 0 & C_v \\ C_u^t & C_v^t & G \end{bmatrix} = \begin{bmatrix} I & 0 & 0 \\ 0 & A & 0 \\ 0 & 0 & I \end{bmatrix} \begin{bmatrix} M & I & 0 \\ I & 0 & 0 \\ C_u^t & \bar{C}_v^t & \bar{G} \end{bmatrix} \begin{bmatrix} I & 0 & \bar{C}_v \\ 0 & I & \bar{C}_u \\ 0 & 0 & I \end{bmatrix} \begin{bmatrix} I & 0 & 0 \\ 0 & A & 0 \\ 0 & 0 & I \end{bmatrix},$$

$$\text{(Eq 3.2)}$$

where

$$A\bar{C}_v = C_v,$$
$$\bar{C}_u = C_u - M\bar{C}_v,$$
$$\bar{G} = G - C_u^t\bar{C}_v - \bar{C}_v^t\bar{C}_u.$$

For each subdomain scalar diffusion coefficient, the computation of $\bar{C}_v$ requires the solution of one linear system with A, while each 2×2 diffusion tensor requires the solution of two or three such linear systems. At the right-hand side of (Eq 3.2), each of the two block-diagonal matrices requires the solution of one linear system with A. It follows that a total of $K_s + 2K_r + 3K_t + 2$ elliptic PDE systems must to be solved at each Newton step, where K_s, K_r, and K_t are the number of scalars, tensors with a known rotation, and those with an unknown rotation respectively, such that $K_s + K_r + K_t = K$. The block lower-triangular system requires the solution of one dense linear system with the low-dimensional symmetric matrix $\bar{G}$.

The overall solution procedure given below is similar to an earlier version of the algorithm described and implemented in the PDE solver package PLTMG [2]. As the linear systems involving A may be solved approximately by iteration, we introduce the matrix $\hat{C}_v \approx \bar{C}_v$, which is generally the approximate $\bar{C}_v$ saved from the previous Newton step. This allows the matrix $\bar{C}_v$ to be updated iteratively at each Newton step. The matrix $\hat{C}_v$ is initially set to zero, and updated at every Newton step.

The first step is to solve

$$A\bar{J}_v = J_v,$$
$$AW = C_v - A\widehat{C}_v,$$
$$\widehat{C}_v \leftarrow \widehat{C}_v + W,$$
$$\bar{C}_v = \widehat{C}_v.$$

All the linear systems involving A are solved approximately using an incomplete LU factorizing (*ILU*) preconditioned conjugate-gradient method. Then we form

$$\bar{J}_u = J_u - M\bar{J}_v,$$
$$\bar{C}_u = C_u - M\bar{C}_v,$$

which requires sparse matrix multiplications with M. The next step is to compute δd using the Schur complement

$$\bar{G} = G - C_u^t \bar{C}_v - \bar{C}_v^t \bar{C}_u,$$
$$\bar{G}\delta d = -(J_d - C_u^t \bar{J}_v - \bar{C}_v^t \bar{J}_u).$$

Finally, δu and δv are formed from

$$\delta u = -(\bar{J}_v + \bar{C}_v \delta d),$$
$$A\delta v = -(\bar{J}_u + \bar{C}_u \delta d).$$

The second equation requires the linear solver for A. This solver is implemented in PLTMG, which is applied to three numerical examples in the next section.

4 Numerical Results

In order to illustrate the numerical stability and computational efficiency of the OPT-PDE approach, the solver was applied to four examples arising from three different scenarios of molecular diffusion in live cells, i.e., spot diffusion, layered diffusion, and filament tensor diffusion. In each of the examples, the forward numerical simulation functions in our Fluocell software package were used to generate input concentration maps of known diffusion maps [25,24]. These concentration maps and their finite element triangulations were read into PLTMG as input for the OPT-PDE model. The diffusion coefficients were then estimated by solving the optimization problem described in (Eq 2.8) using the OPT-PDE algorithm of PLTMG, which implements the method described in Section 3. The computed diffusion coefficients were compared with the known diffusion map to determine the accuracy and efficiency of the OPT-PDE solver. The PLTMG OPT-PDE solver was run on an Apple Mac Pro Laptop computer with an intel i5 dual-core processor (2.9 GHz) and 8GB RAM.
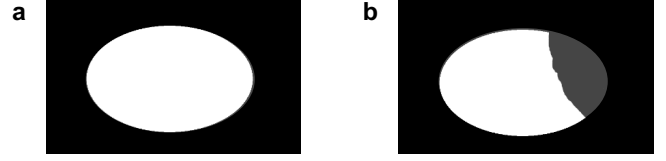
Fig. 4.1: **The cell model and the photobleaching pattern used in the simulation.** (a) The basic geometry of the cell model (white) used for the spot diffusion and filament tensor diffusion simulation. (b) shows the subcellular region to be photobleached in dark gray.

In the forward simulation, a certain region in an elliptic cell model is designated as the photobleached region (see Figure 4.1), which represents the subcellular region with lower initial concentration at time $t = 0s$. A diffusion map on the cell model is designated to be piecewise constant with assigned values on a given subdomain structure (e.g., Figure 4.2a). A computer simulation was then performed to mimic the fluorescence recovery after photobleaching (FRAP) process via diffusion (Figure 4.2b) [25].

The OPT-PDE algorithm has a three levels of iterations. At the top level, a sequence of "rounds" are performed in which the optimization problem is solved with the regularization term $d - d_0$ defined with d_0 the solution of the problem from the previous round. The next level of iterations are those of Newton's method applied to the discretized first-order optimality conditions. At the lowest level, the iterations are those of the method used to solve the KKT equations (Eq 3.1).

4.1 Spot Diffusion

Under the assumption that intra-cellular molecules diffuse more slowly in certain subcellular regions, smaller diffusion coefficients were assigned to four small elliptic or circular sub-cellular regions within the cell body. The corresponding diffusion map and finite element triangulation were generated accordingly (Figure 4.2a), with the photobleach pattern shown in (Figure 4.1b). The forward diffusion simulator of Fluocell was used to simulate FRAP, with the simulated concentration u_1, u_2, and scaled change of concentration $u_2 - u_1$ shown in (Figure 4.2b). The change of concentration $u_2 - u_1$, was scaled by multiplying the factor $s = (\max_x(u_1, u_2) - \min_x(u_1, u_2))^{-1}$, such that its magnitude is less or equal to 1. The new solver implemented in PLTMG takes the forward simulation results as an input and the concentration and diffusion maps are estimated by multiple rounds of OPT-PDE solving (Figure 4.3)[2]. The

regularization constant is $\gamma = 10^{-5}$ for all three test problems. Alternatively, it is possible to adjust the values of γ at each round of OPT-PDE solve, which may potentially speed up convergence, although this approach was not adopted in our solver. For all the test problems, the lower and upper bounds for the diffusion coefficients are $d_{\min} = 0.1\,\mu m^2/s$ and $d_{\max} = 500\,\mu m^2/s$.

For the first round of OPT-PDE solves, the initial guess of the diffusion coefficients were $10\,\mu m^2/s$ for all subcellular regions, which was implemented into the solver as $d_{1,0}$ and $d_{2,0}$ in the regularization term of the objective function. It took four steps for Newton's method to converge to the optimal solution, with a Newton increment larger than or equal to 10^{-2} and the residual decreasing until it was smaller than 10^{-5} (Figure 4.3(a)). The PDE was discretized using finite element method, and the resulting linear system involving the stiffness matrix A was solved using incomplete LU factorization [2, 4]. There were 3882 mesh nodes, and it took 1.23 s to solve each linear system, with majority (about 69.2%) of time spent on assembling the stiffness and mass matrices (Figure 4.3b). As there were two different scalar diffusion coefficients, four solves of the PDE were needed for each Newton's iteration. The computing time necessary to solve a single PDE is estimated to be $0.18s$, and the overall computing time is $5.15s$, which is a 29-fold increase over the cost of a single solve. The diffusion coefficients converged to $d_1 = 27.4\,\mu m^2/s$ and $d_2 = 6.79\,\mu m^2/s$ at the end of the 1st round of the OPT-PDE solver (see Figure 4.3c).

In the 2nd round of the OPT-PDE solver, the estimates $d_{1,0}$ and $d_{2,0}$ were set to the solutions from the first OPT-PDE solve, which provide an improved estimation of the optimal diffusion coefficients (Eq 2.8). By iteratively improving the regularization term in the objective function, the OPT-PDE solver converges at round 6, when the increments in the diffusion coefficients were less than 1% of their initial values (see Figure 4.3c). The solutions of diffusion coefficients are recorded as d_1^* and d_2^*. The convergence process of the relative diffusion coefficients d_1/d_1^* and d_2/d_2^* are shown in Figure 4.3d. These results show that the optimized solution of d is accurate, and that both diffusion coefficients converged with similar efficiency, as intended by the normalized regularization terms in (Eq 2.8). In addition, we can estimate the optimal Lagrange multiplier v^h and the scaled solution of $u - u_1$ (Figures 4.3e and 4.3f). The solution $u - u_1$ was scaled in the same way as the input change of concentration, $u_2 - u_1$, as shown in Figure 4.2b. The results given in Figures 4.2b and 4.3f) indicate that the scaled $u - u_1$ approximates the scaled $u_2 - u_1$ very well.

In order to demonstrate the need for the regularization term, a model problem was constructed where the KKT matrix is singular, or the discrete Laplacian of the solution is zero in certain local regions. In this case, a nonzero regularization term is necessary to ensure that the discrete op-

timization problem is well-posed. As in the forward simulation results shown in Figure 4.3, the diffusion map, triangulation, u_1, u_2, and scaled $u_1 - u_2$ are shown in Figure 4.4. If the regularization constant γ is zero and the initial estimate of the diffusion coefficients was $10\,\mu m^2/s$, Newton's method was unable to compute a solution. However, for $\gamma = 10^{-5}$, the solver converged successfully to $d_1 = 29\,\mu m^2/s$, $d_2 = 5\,\mu m^2/s$. In this case d_3 converged to the initial estimate $10\,\mu m^2/s$ because of the lack of information provided by the diffusion equation (see Figure 4.5). These results show that the regularization term is necessary to ensure that the optimization problem is well-posed when the KKT matrix is rank deficient. Regularization can also be used to improve the rate of convergence and robustness of the solver when an optimization problem is well-posed, or when the block Gaussian elimination is too expensive to compute (see, e.g., [29]). Therefore, the proposed theoretical and numerical framework can serve as a foundation for solving a wider class of optimization problems with PDE constraints.

4.2 Layered Diffusion

In the second example, the cell model was divided into four layers in the axial direction, with four different scalar diffusion coefficients (see Figure 4.6a). The photobleach pattern was defined to allow the bleached region encompass all four layers (Figure 4.6b). Again, forward simulation of the diffusion process was performed to generate the concentration maps u_1 and u_2 at different time points after photobleaching, as well as the scaled change of concentration $u_2 - u_1$ (Figure 4.6c). These simulation results, but not the diffusion map, were then used as input for the OPT-PDE solver in PLTMG to estimate the diffusion map given in Figure 4.7.

Similar to the first numerical example, PLTMG took the forward simulation results as input and estimated the concentration and diffusion maps by multiple rounds of OPT-PDE solving, with $\gamma = 10^{-5}$ and adaptive regularization terms in the objective functions. For the initial round of OPT-PDE solve, the initial guess of the diffusion coefficients were again $10\,\mu m^2/s$ for all subcellular regions. There were 6820 mesh nodes, and it took 2.38 s to solve each PDE problem (Figure 4.7b). The computing time necessary to solve a single PDE is estimated to be $0.38s$, and the overall computing time is $6.59s$, which is a 17-fold increase over the cost of a single solve. For each Newton iteration, six solves of the PDE were needed to compute the four diffusion coefficients. Each Newton iteration required 4 steps to converge to the optimal solution of the objective (Figure 4.7(a)). The OPT-PDE solver converged at round 3 (Figure 4.7c), with the diffusion coefficients converges to d_1^*, d_2^*, d_3^* and d_4^*. The convergence of the relative diffusion coefficients d_i/d_i^*
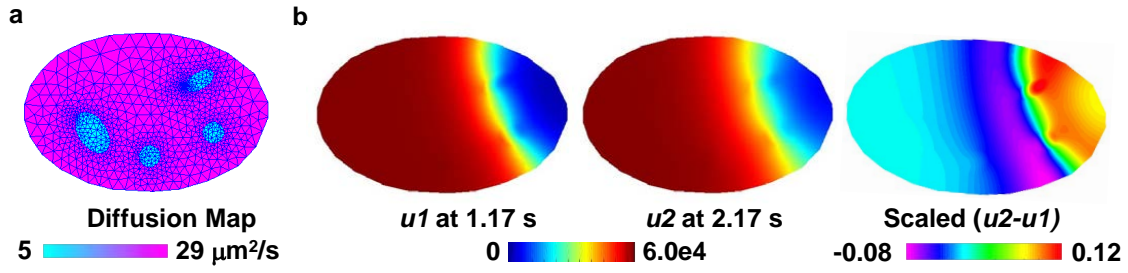
Fig. 4.2: **Forward simulation results.** (a) The diffusion map for spot diffusion overlaid with the finite element mesh. The diffusion coefficient of the large cell body area was assigned to be $\bar{d}_1 = 29\,\mu m^2/s$, while that of the small elliptic regions was $\bar{d}_2 = 5\,\mu m^2/s$. (b) The left and middle figures depict the simulated concentration maps of the diffusing molecules at different time points after photobleaching. The right figure gives the scaled concentration map $u_2 - u_1$ used as the input for the OPT-PDE solver.
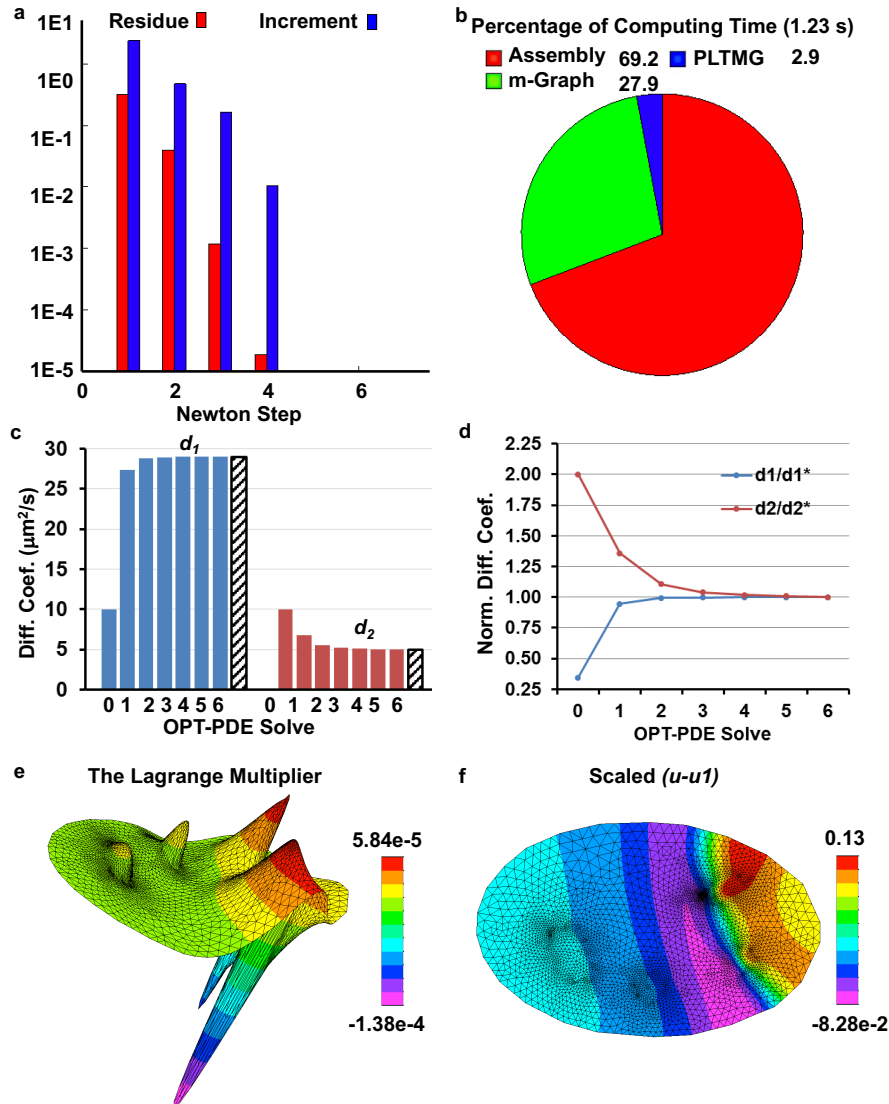

Fig. 4.3: **The OPT-PDE solution for the spot diffusion problem.** At the initial round of the OPT-PDE solve, (a) shows the Newton increments and residuals (logarithmic scale) vs the number of Newton steps; (b) shows the time for each Newton iteration displayed as a pie graph that gives the percentage of time used by each component of the solver. (c) The optimal diffusion coefficients after each round of OPT-PDE solves. The exact values of $\bar{d}_1$ and $\bar{d}_2$ used in the forward simulation are plotted in black/white stripes as the reference. (d) The normalized diffusion coefficients are shown versus the OPT-PDE solving rounds. d_1^* and d_2^* are the optimal solutions of diffusion coefficients after convergence. (e) The Lagrange multiplier. (f) The scaled solution of $u - u_1$.

a

Diffusion Map

5 ▮ 29 μm²/s

b

u1 at 10.08 s

0 ▮ 6.0e4

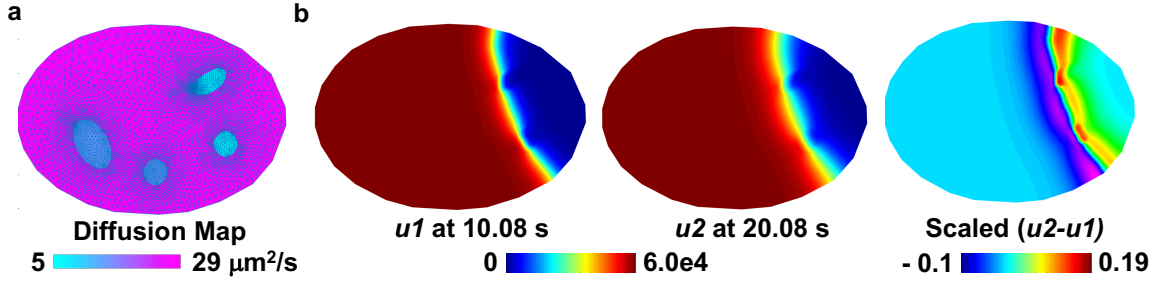*u2* at 20.08 s

Scaled (*u2-u1*)

- 0.1 ▮ 0.19

Fig. 4.4: **Forward simulation results. (a)** The diffusion map for spot diffusion overlaid with the finite element mesh. The diffusion coefficient of the large cell body area was assigned to be $\bar{d}_1 = 29\,\mu m^2/s$, while those of the two small elliptic regions at the right side were each $\bar{d}_2 = 5\,\mu m^2/s$. The diffusion coefficients of the two small regions on the left were both $\bar{d}_2 = 15\,\mu m^2/s$. **(b)** The left and middle figures give the simulated concentration maps of the diffusing molecules at different time points after photobleaching. The right figure gives the scaled concentration map $u_2 - u_1$ used as the input for the OPT-PDE solver.
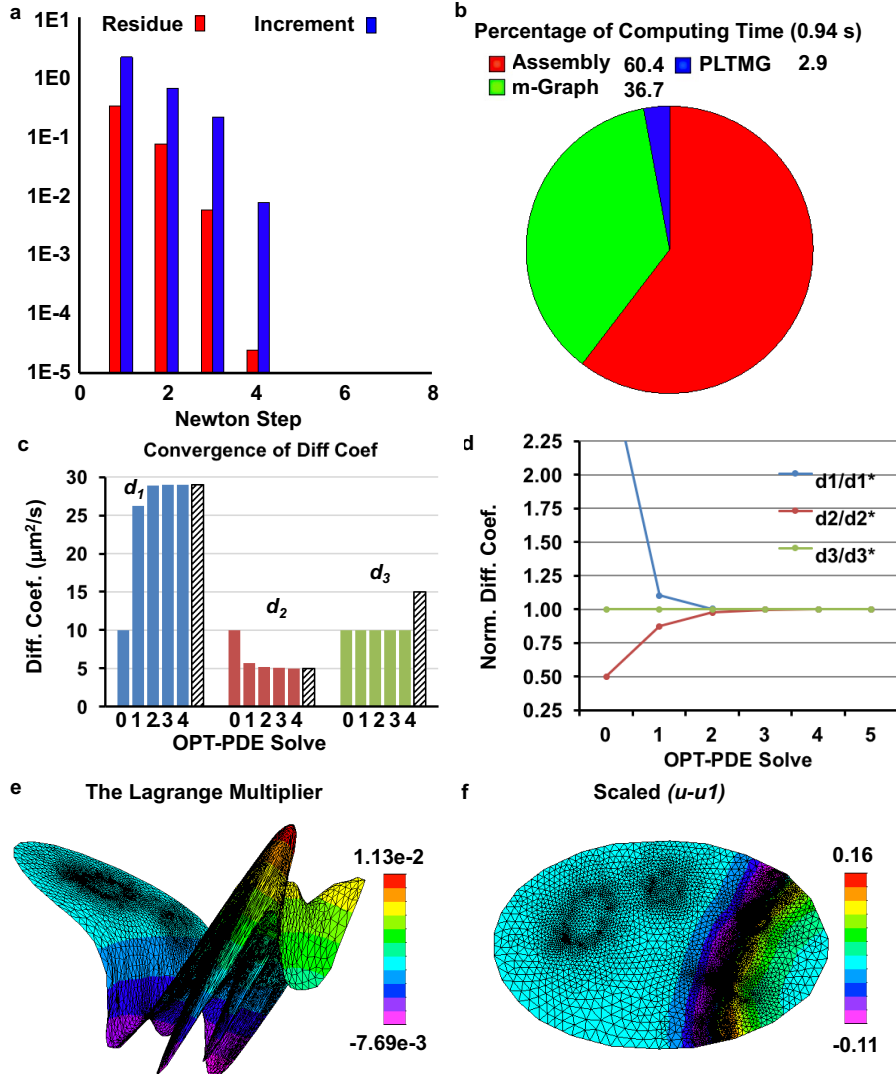
a

Residue ▮   Increment ▮

1E1
1E0
1E-1
1E-2
1E-3
1E-4
1E-5

0   2   4   6   8
Newton Step

b

Percentage of Computing Time (0.94 s)

▮ Assembly 60.4 ▮ PLTMG 2.9
▮ m-Graph   36.7

c

Convergence of Diff Coef

d_1 d_2 d_3

Diff. Coef. (μm²/s)

0 1 2 3 4   0 1 2 3 4   0 1 2 3 4
OPT-PDE Solve

d

2.25
2.00
1.75
1.50
1.25
1.00
0.75
0.50
0.25

d1/d1*
d2/d2*
d3/d3*

Norm. Diff. Coef.

0   1   2   3   4   5
OPT-PDE Solve

e

The Lagrange Multiplier

1.13e-2

-7.69e-3

f

Scaled *(u-u1)*

0.16

-0.11

Fig. 4.5: **The OPT-PDE solution for the spot diffusion problem with necessary Tikohnov regularization.** At the initial round of OPT-PDE solve, **(a)** shows the Newton increments and residuals (logarithmic scale) vs the number of Newton steps; **(b)** shows the computing time of each Newton iteration displayed in the pie graph showing the percentage of time used by each solver component. **(c)** The optimal diffusion coefficients after each round of OPT-PDE solve. The exact values of $\bar{d}_1$, $\bar{d}_2$, and $\bar{d}_2$ used in forward simulation are plotted in black/white stripes as the reference. **(d)** The normalized diffusion coefficients are shown versus the OPT-PDE solving rounds. d_1^*, d_2^*, and d_3^* are the optimal solutions of diffusion coefficients after convergence. **(e)** The Lagrange multiplier. **(f)** The scaled solution $u - u_1$.
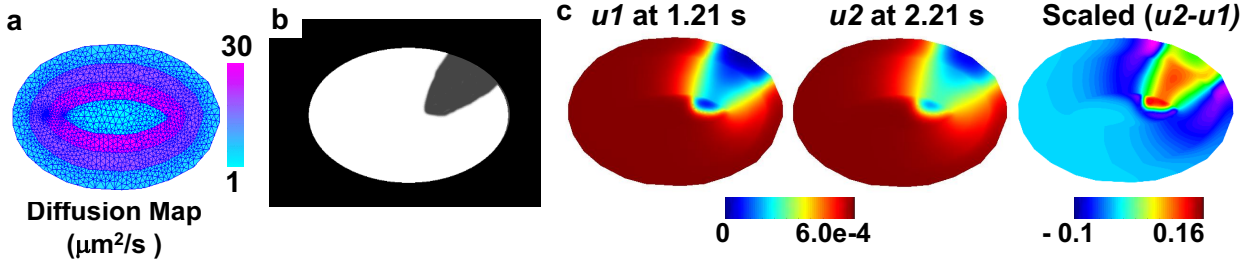
Fig. 4.6: **Forward simulation results.** (a) The diffusion map for layered diffusion overlaid with the finite element mesh. Moving from the outside to the inside, the diffusion coefficients of the four layers are $\bar{d}_1 = 5\,\mu m^2/s$, $\bar{d}_2 = 20\,\mu m^2/s$, $\bar{d}_3 = 30\,\mu m^2/s$, and $\bar{d}_4 = 1\,\mu m^2/s$. Panel (b) shows the photobleach pattern in gray. (c) The left and middle figures give the simulated concentration maps of the diffusing molecules at different time points after photobleaching. The right figure depicts the scaled concentration map $u_2 - u_1$ used as the input for the OPT-PDE solver.
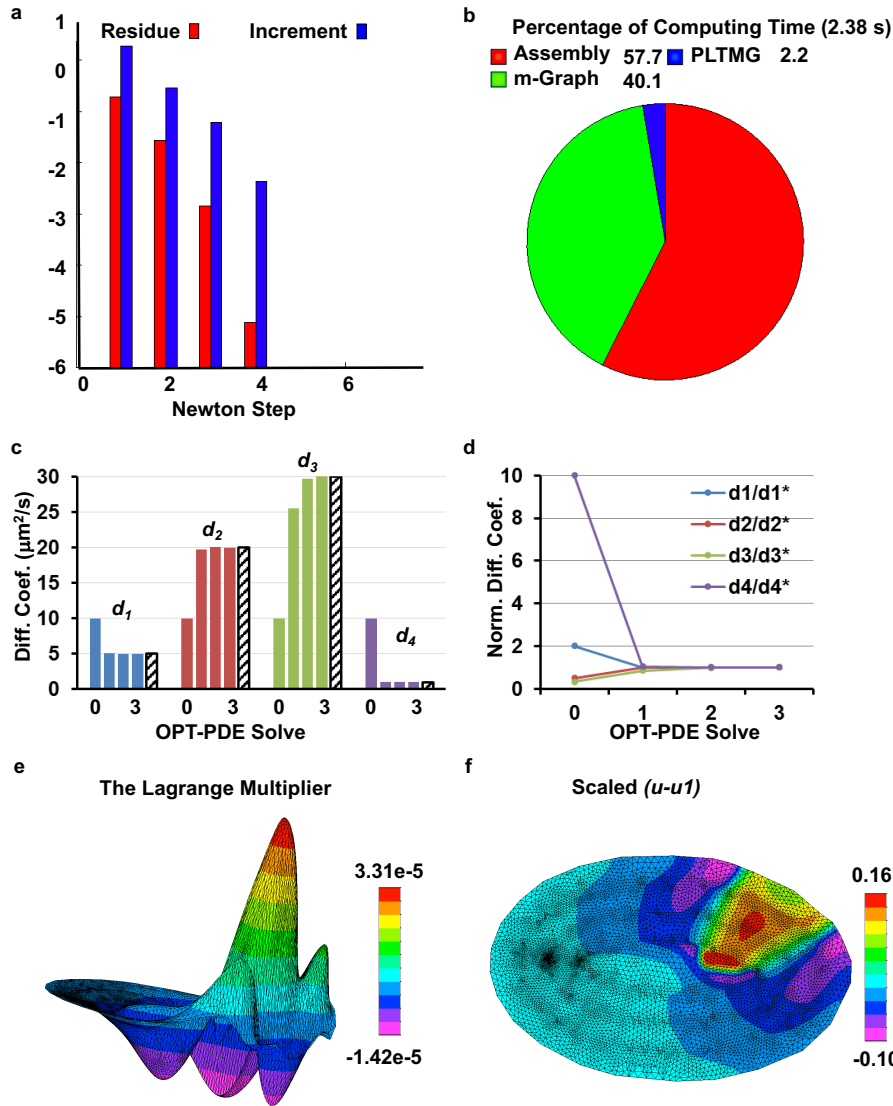

Fig. 4.7: **The OPT-PDE solution for the spot diffusion problem.** At the initial round of OPT-PDE solve, (a) shows the Newton increments and residuals (logarithmic scale) vs. the number of Newton steps; (b) shows the computing time of each Newton iteration displayed in the pie graph showing the percentage of time used by each solver component. (c) The optimal diffusion coefficients after each round of the OPT-PDE solve. The accurate values of $\bar{d}_i$, $i = 1, 2, 3, 4$ used in forward simulation are plotted in black/white stripes as a reference. (d) The normalized diffusion coefficients are shown vs the OPT-PDE solving rounds. d_i^*, $i = 1, 2, 3, 4$ are the optimal solutions at convergence. (f) The Lagrange multiplier. (g) The scaled solution of $u - u_1$.

is shown in Figure 4.7d, indicating that all diffusion coefficients converged with similar efficiency. In addition, we estimated the optimal Lagrange multiplier ν^h and confirmed that the scaled solution of $u - u_1$ approximates the scaled change of concentration, $u_2 - u_1$ (Figures 4.6c and 4.7e-f).

4.3 Filament Tensor Diffusion

In cells, it is possible that anisotropic diffusion can occur along the long axis of certain filamentous structures. To study the applicability of our solver to such scenarios, we designed a diffusion map with two independent filaments, where the diffusion coefficients were set to be isotropic in the general cell model and anisotropic on the filaments (Figure 4.8(a)). The diffusion tensor was calculated using the transformation matrix based on the known orientations of the filaments (Figure 4.8a). The same photobleach pattern from spot diffusion simulation was used (4.1b). As such, we utilized the known orientation of the filaments to construct the finite element mesh, simulated locally anisotropic diffusion and the resulting concentration maps. These, but not the diffusion map, were used as input to test the OPT-PDE solver in PLTMG.

As in the previous examples, PLTMG took the forward simulation results as input and were able to estimate the concentration and diffusion maps by ten rounds of OPT-PDE solve (Figure 4.9), with adaptive objective functions. The initial guess of the diffusion coefficients were again $10\,\mu m^2/s$ for all directions and subcellular regions. In the initial round of OPT-PDE solve, Newton's iteration took four steps to converge (Figure 4.9(a)). There were 3919 mesh nodes, and it took $1.31s$ to solve each PDE problem (see Figure 4.9b). The computing time necessary to solve a single PDE is estimated to be $0.21s$, and the overall computing time is $12.64s$, which is a 60-fold increase over the cost of a single solve. Each Newton iteration required five solves of the PDE for the three diffusion components. At the 10th round of the PDE-OPT solve (Figure 4.9c), the diffusion coefficients converges to d_1^*, d_2^*, and d_3^*. The convergence of the relative diffusion coefficients d_i/d_i^* is shown in Figure 4.9d, indicating that d_1/d_1^* and d_3/d_3^* converged at a similar rate while d_2/d_2^* was slower to converge. The different convergence rates may be caused by the small size of the filaments relative to the cell body, as well as the 20-fold difference in the diffusion rate along the filament compared to the cell body. The optimal Lagrange multiplier ν^h is given in Figure 4.9e). The scaled solution $u - u_1$, which approximates the scaled change of concentration $u_2 - u_1$, is depicted in Figures 4.8c and 4.9f.

Taken together, the numerical simulation and solution results demonstrate that the proposed OPT-PDE solver provides a highly accurate, computationally efficient, and numerically robust tool for estimating the spatial diffusion maps in both isotropic and anisotropic problems.

5 Discussion and Future Work

In this work, we consider the solution of biologically motivated inverse problems associated with spatially heterogeneous diffusion coefficients based on known concentration maps. The problem is formulated as an optimization problem with the diffusion equation as a constraint. The well-posedness of both the PDE and the optimization model is established. Newton's method is used to solve the finite-dimensional optimization problem obtained by discretizing the PDE with finite elements in space and finite differences in time. An efficient OPT-PDE solver is formulated that exploits the special algebraic structure of the finite-element stiffness and mass matrices. Finally, numerical examples are presented that demonstrate the robust and efficient convergence of the solver for three example problems with spatially discontinuous or anisotropic diffusion coefficients. These results indicate that the proposed OPT-PDE approach for finding the diffusion coefficients is accurate and robust, and it may be used for cellular image-based analysis to reconstruct molecular transport parameters.

The ultimate goal of this work is to develop an OPT-PDE analysis framework that can be used to reveal the spatiotemporal map of molecular diffusion and transport in live cells with high resolution. Therefore, a future research direction is to generalize the OPT-PDE solver to imaging problems. The OPT-PDE solver itself can be developed to allow the diffusion map to be a piecewise linear function on the domain without knowing the specific geometric configuration of the subdomains. The PDE constraint can be a sophisticated reaction-diffusion system, from 2D to 3D model problems, or directly from bio-imaging data. In summary, we envision significant bio-imaging applications for this class of OPT-PDE models and a great potential to explore and develop new functionality for the solver.

6 References

References

1. Axelrod, D., Koppel, D.E., Schlessinger, J., Elson, E., Webb, W.W.: Mobility measurement by analysis of fluorescence photobleaching recovery kinetics. Biophys J **16**(9), 1055–69 (1976). URL http://www.ncbi.nlm.nih.gov/pubmed/786399. DOI 10.1016/S0006-3495(76)85755-4
2. Bank, R.E.: Pltmg: A software package for solving elliptic partial differential equations, user guide 11.0. Technical Report, Department of Mathematics, University of California, San Diego (2012)
3. Bank, R.E., Gill, P.E., Marcia, R.F.: Interior methods for a class of elliptic variational inequalities. In: Large-scale PDE-constrained optimization (Santa Fe, NM, 2001), *Lect. Notes Comput. Sci. Eng.*,
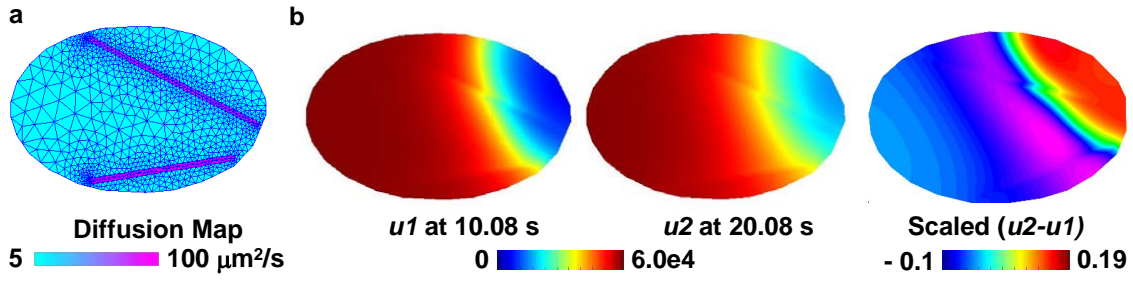
Fig. 4.8: **Forward simulation results for filament tensor diffusion.** (a) The diffusion map with the magnitudes of the tensor diffusion vectors overlaid with the finite element mesh. The diffusion coefficients were set to be $\bar{d}_1 = 5\,\mu m^2/s$ in the general cell area, $\bar{d}_2 = 100\,\mu m^2/s$ along the filaments, and $\bar{d}_3 = 5\,\mu m^2/s$ perpendicular to the filaments. (b) The left and middle figures give the simulated concentration maps of the diffusing molecules at different time points after photo-bleaching. The right figure gives the scaled concentration map $u_2 - u_1$ used as the input for the OPT-PDE solver.
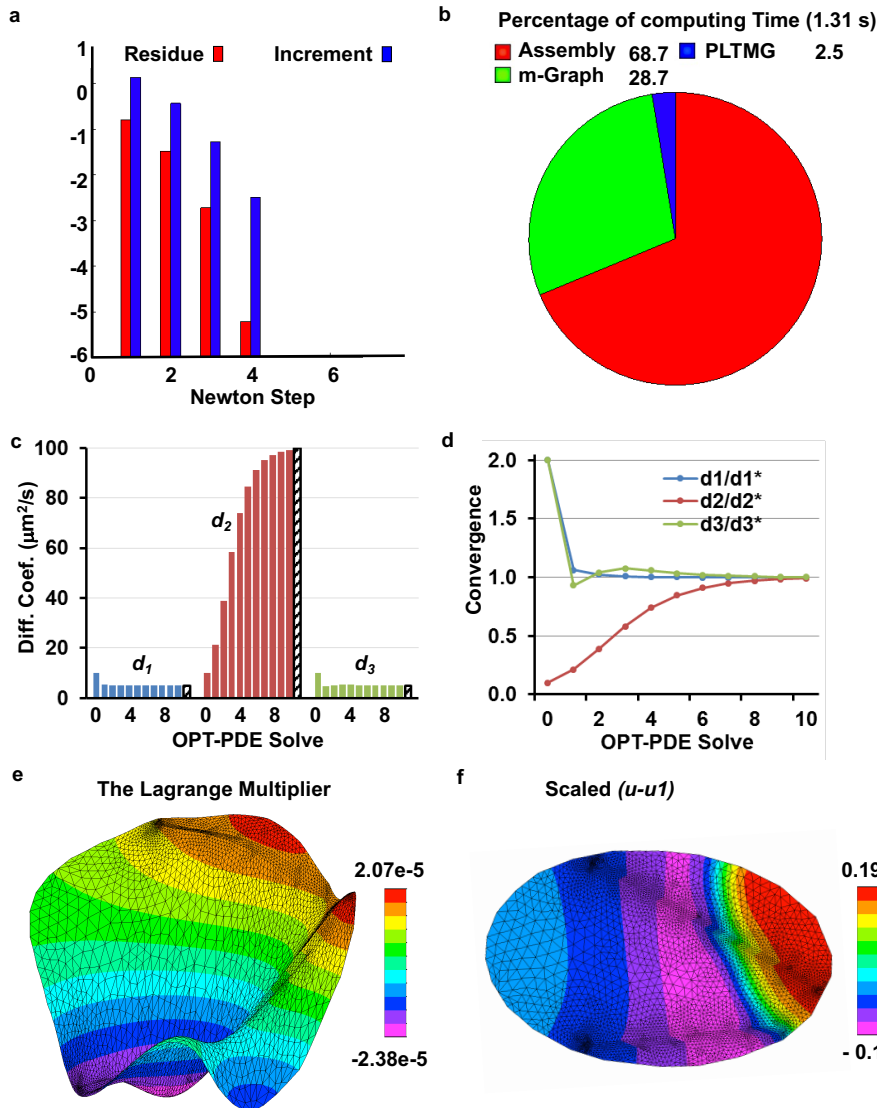

Fig. 4.9: **The OPT-PDE solution for the filament tensor diffusion problem.** At the initial round of OPT-PDE solve, (a) shows the Newton increments and residuals (logarithmic scale) vs the number of Newton steps; (b) shows the computing time of each Newton iteration displayed in the pie graph showing the percentage of time used by each solver component. (c) The optimal diffusion coefficients after each round of OPT-PDE solve. The accurate values of $\bar{d}_i$, $i = 1, 2, 3$ used in forward simulation are plotted in black/white stripes as a reference. (d) The normalized diffusion coefficients are shown versus the OPT-PDE solving rounds. d_i^*, $i = 1, 2, 3$ are the optimal values after convergence. (f) The Lagrange multiplier. (g) The scaled solution $u - u_1$.

vol. 30, pp. 218–235. Springer, Berlin (2003). DOI 10.1007/ 978-3-642-55508-4_13

4. Bank, R.E., Smith, R.K.: An algebraic multilevel multigraph algorithm. SIAM J. Sci. Comput. **23**(5), 1572–1592 (electronic) (2002). DOI 10.1137/S1064827500381045

5. Biros, G., Ghattas, O.: Parallel Lagrange-Newton-Krylov-Schur methods for PDE-constrained optimization. I. The Krylov-Schur solver. SIAM J. Sci. Comput. **27**(2), 687–713 (electronic) (2005). DOI 10.1137/S106482750241565X

6. Brenner, S.C., Scott, L.R.: The mathematical theory of finite element methods, *Texts in Applied Mathematics*, vol. 15, second edn. Springer-Verlag, New York (2002). DOI 10.1007/ 978-1-4757-3658-8

7. Capoulade, J., Wachsmuth, M., Hufnagel, L., Knop, M.: Quantitative fluorescence imaging of protein diffusion and interaction in living cells. Nat Biotechnol **29**(9), 835–9 (2011). URL http://www.ncbi.nlm.nih.gov/pubmed/21822256. DOI 10. 1038/nbt.1928

8. Cebecauer, M., Spitaler, M., Serge, A., Magee, A.I.: Signalling complexes and clusters: functional advantages and methodological hurdles. J Cell Sci **123**(Pt 3), 309–20 (2010). URL http:// www.ncbi.nlm.nih.gov/pubmed/20130139. DOI 10.1242/jcs. 061739

9. Crank, J.: The Mathematics of Diffusion, Second edn. Clarendon Press, Oxford (1975)

10. Dryja, M., Sarkis, M.V., Widlund, O.B.: Multilevel Schwarz methods for elliptic problems with discontinuous coefficients in three dimensions. Numer. Math. **72**(3), 313–348 (1996). DOI 10.1007/ s002110050172

11. Gill, P.E., Murray, W., Saunders, M.A.: SNOPT: an SQP algorithm for large-scale constrained optimization. SIAM Rev. **47**(1), 99–131 (electronic) (2005). DOI 10.1137/S0036144504446096

12. Gockenbach, M.S., Khan, A.A.: An abstract framework for elliptic inverse problems. I. An output least-squares approach. Math. Mech. Solids **12**(3), 259–276 (2007). URL http://dx.doi.org/ 10.1177/1081286505055758. DOI 10.1177/1081286505055758

13. Groves, J.T., Kuriyan, J.: Molecular mechanisms in signal transduction at the membrane. Nat Struct Mol Biol **17**(6), 659–65 (2010). URL http://www.ncbi.nlm.nih.gov/pubmed/ 20495561. DOI 10.1038/nsmb.1844

14. Haber, E., Hanson, L.: Model problems in PDE-constrained optimization. Report, Emory University (2007)

15. Herzog, R., Kunisch, K.: Algorithms for PDE-constrained optimization. GAMM-Mitt. **33**(2), 163–176 (2010)

16. Hinze, M., Pinnau, R., Ulbrich, M., Ulbrich, S.: Optimization with PDE constraints, *Mathematical Modelling: Theory and Applications*, vol. 23. Springer, New York (2009)

17. Hoppe, R.H.W., Petrova, S.I., Schulz, V.: Primal-dual Newton-type interior-point method for topology optimization. J. Optim. Theory Appl. **114**(3), 545–571 (2002). DOI 10.1023/A: 1016070928600

18. Jittorntrum, K.: An implicit function theorem. J. Optim. Theory Appl. **25**(4), 575–577 (1978). DOI 10.1007/BF00933522

19. Kellogg, R.B.: On the Poisson equation with intersecting interfaces. Applicable Anal. **4**, 101–129 (1974/75). Collection of articles dedicated to Nikolai Ivanovich Muskhelishvili

20. Kinkhabwala, A., Bastiaens, P.I.: Spatial aspects of intracellular information processing. Curr Opin Genet Dev **20**(1), 31–40 (2010)

21. Klonis, N., Rug, M., Harper, I., Wickham, M., Cowman, A., Tilley, L.: Fluorescence photobleaching analysis for the study of cellular dynamics. Eur Biophys J **31**(1), 36–51 (2002). URL http:// www.ncbi.nlm.nih.gov/pubmed/12046896

22. Knowles, I.: Parameter identification for elliptic problems. J. Comput. Appl. Math. **131**(1-2), 175–194 (2001). URL http:// dx.doi.org/10.1016/S0377-0427(00)00275-2. DOI 10.1016/ S0377-0427(00)00275-2

23. Lippincott-Schwartz, J., Altan-Bonnet, N., Patterson, G.H.: Photobleaching and photoactivation: following protein dynamics in living cells. Nat Cell Biol **Suppl**, S7–14 (2003). URL http: //www.ncbi.nlm.nih.gov/pubmed/14562845

24. Lu, S., Kim, T.J., Chen, C.E., Ouyang, M., Seong, J., Liao, X., Wang, Y.: Computational analysis of the spatiotemporal coordination of polarized pi3k and rac1 activities in micro-patterned live cells. PLoS One **6**(6), e21,293 (2011). DOI 10.1371/journal.pone. 0021293

25. Lu, S., Ouyang, M., Seong, J., Zhang, J., Chien, S., Wang, Y.: The spatiotemporal pattern of src activation at lipid rafts revealed by diffusion-corrected fret imaging. PLoS Comput Biol **4**(7), e1000,127 (2008). URL http://www.ncbi.nlm.nih.gov/entrez/query.fcgi?cmd= Retrieve&db=PubMed&dopt=Citation&list_uids=18711637

26. Nocedal, J., Wright, S.J.: Numerical optimization, second edn. Springer Series in Operations Research and Financial Engineering. Springer, New York (2006)

27. Ortega, J.M., Rheinboldt, W.C.: Iterative solution of nonlinear equations in several variables. Society for Industrial and Applied Mathematics (SIAM), Philadelphia, PA (2000). Reprint of the 1970 original

28. Oswald, P.: On the robustness of the BPX-preconditioner with respect to jumps in the coefficients. Math. Comp. **68**(226), 633–650 (1999). DOI 10.1090/S0025-5718-99-01041-8

29. Parikh, N., Boyd, S.: Proximal algorithms. Foundations and Trends in Optimization **1**(3), 127–239 (2014). URL http://dx. doi.org/10.1561/2400000003. DOI 10.1561/2400000003

30. Petzoldt, M.: Regularity and error estimators for elliptic problems with discontinuous coefficients. Ph.D. thesis, Weierstrass Institute for Applied Analysis and Stochastics (2001)

31. Petzoldt, M.: Regularity results for Laplace interface problems in two dimensions. Z. Anal. Anwendungen **20**(2), 431–455 (2001). DOI 10.4171/ZAA/1024

32. Petzoldt, M.: A posteriori error estimators for elliptic equations with discontinuous coefficients. Adv. Comput. Math. **16**(1), 47–75 (2002). DOI 10.1023/A:1014221125034

33. Press, W.H., Teukolsky, S.A., Vetterling, W.T., Flannery, B.P.: Numerical recipes, third edn. Cambridge University Press, Cambridge (2007). The art of scientific computing

34. Rockafellar, R.T.: Augmented Lagrangians and applications of the proximal point algorithm in convex programming. Mathematics of operations research **1**(2), 97–116 (1976)

35. Scott, J.D., Pawson, T.: Cell signaling in space and time: where proteins come together and when they're apart. Science **326**(5957), 1220–4 (2009). URL http://www.ncbi.nlm.nih. gov/pubmed/19965465

36. Sniekers, Y.H., van Donkelaar, C.C.: Determining diffusion coefficients in inhomogeneous tissues using fluorescence recovery after photobleaching. Biophys J **89**(2), 1302–7 (2005). URL http://www.ncbi.nlm.nih.gov/pubmed/15894637. DOI 10. 1529/biophysj.104.053652

37. Tikhonov, A.N., Goncharsky, A.V., Stepanov, V.V., Yagola, A.G.: Numerical methods for the solution of ill-posed problems, *Mathematics and its Applications*, vol. 328. Kluwer Academic Publishers Group, Dordrecht (1995). Translated from the 1990 Russian original by R. A. M. Hoksbergen and revised by the authors, DOI 10.1007/978-94-015-8480-7

38. Van Beusekom, A.E., Parker, R.L., Bank, R.E., Gill, P.E., Constable, S.: The 2-d magnetotelluric inverse problem solved with optimization. Geophysical Journal International **184**(2), 639–650 (2011). DOI 10.1111/j.1365-246X.2010.04895.x

39. Xu, J.: Iterative methods by space decomposition and subspace correction. SIAM Rev. **34**(4), 581–613 (1992). DOI 10.1137/ 1034116

40. Yu, S.R., Burkhardt, M., Nowak, M., Ries, J., Petrasek, Z., Scholpp, S., Schwille, P., Brand, M.: Fgf8 morphogen gradient forms by a source-sink mechanism with freely diffusing molecules. Nature **461**(7263), 533–6 (2009). URL http://www.ncbi.nlm.nih.gov/pubmed/19741606. DOI 10.1038/nature08391

41. Zeidler, E.: Nonlinear functional analysis and its applications. I. Springer-Verlag, New York (1986). Fixed-point theorems, Translated from the German by Peter R. Wadsack, DOI 10.1007/978-1-4612-4838-5

42. Zheng, H., Wu, J.: Convergence analysis on multigrid methods for elliptic problems with large jumps in coefficients. IMA J. Numer. Anal. **35**(4), 1888–1912 (2015). DOI 10.1093/imanum/dru055

43. Zou, J.: Numerical methods for elliptic inverse problems. Int. J. Comput. Math. **70**(2), 211–232 (1998). URL http://dx.doi.org/10.1080/00207169808804747. DOI 10.1080/00207169808804747